

Periodontal Bone Loss Analysis via Keypoint Detection With Heuristic Post-Processing

Ryan Banks ^a, Vishal Thengane ^a, María Eugenia Guerrero ^b, Nelly
Maria García-Madueño ^c, Yunpeng Li ^d, Hongying Tang ^a, Akhilanand
Chaurasia ^e

^aUniversity of Surrey, Guildford, United Kingdom

^bUniversidad Nacional Mayor de San Marcos, Lima, Peru

^cUniversidad de San Martín de Porres, Lima, Peru

^dKing's College London, London, United Kingdom

^eKing George's Medical University, Lucknow, India

Abstract

Calculating percentage bone loss is a critical test for periodontal disease staging but is sometimes imprecise and time consuming when manually calculated. This study evaluates the application of a deep learning keypoint and object detection model, YOLOv8-pose, for the automatic identification of localised periodontal bone loss landmarks, conditions and staging. YOLOv8-pose was fine-tuned on 193 annotated periapical radiographs. We propose a keypoint detection metric, Percentage of Relative Correct Keypoints (PRCK), which normalises the metric to the average tooth size of teeth in the image. We propose a heuristic post-processing module that adjusts certain keypoint predictions to align with the edge of the related tooth, using a supporting instance segmentation model trained on an open-source auxiliary dataset. The model can sufficiently detect bone loss keypoints, tooth boxes, and alveolar ridge resorption, but has insufficient performance at detecting detached periodontal ligament and furcation involvement. The model with post-processing demonstrated a PRCK 0.25 of $0.726(\pm 0.045)$ and PRCK 0.05 of $0.401(\pm 0.050)$ for keypoint detection, mAP 0.5 of $0.715(\pm 0.296)$ for tooth object detection, mesial dice score of $0.593(\pm 0.033)$ for periodontal staging, and dice score of $0.280(\pm 0.098)$ for furcation involvement. Our annotation methodology provides a stage agnostic approach to periodontal disease detection, by ensuring most keypoints are present for each tooth in the image, allowing small imbalanced datasets. Our PRCK metric allows accurate evaluation of keypoints in dental domains. Our post-processing module adjusts

predicted keypoints correctly but is dependent on a minimum quality of prediction by the pose detection and segmentation models. Code: <https://anonymous.4open.science/r/Bone-Loss-Keypoint-Detection-Code>. Dataset: <https://bit.ly/4hJ3aE7>.

Keywords:

Periodontal Bone Loss, Object Detection, Keypoint Detection, AI in Dentistry

1. Introduction

Periodontal bone loss refers to the degradation and loss of the alveolar bone surrounding the teeth, primarily due to periodontal disease [1]. These diseases are inflammatory conditions that affect the oral cavity and range from gingivitis to periodontitis, which result in both soft and hard tissue loss. Periodontal bone loss is a significant indicator of periodontal health and, if not detected and managed in a timely manner, can lead to tooth loss [2].

Traditional diagnostic methods rely on physical probing [3] and radiographic evaluation, typically involving periapical radiographs for the estimation of percentage bone loss [4]. However, these methods require time-consuming expert interpretation and may introduce variability in diagnosis. Given these limitations, the integration of deep learning in radiology-based periodontal diagnostics could provide an accurate, efficient, and cost-effective assessment of bone health [2]. The challenge in adopting these automated approaches is ensuring clinical interpretability, readability, and error identification.

In this study, we investigate the application of a deep learning model to improve the detection of periodontal bone loss. Our approach involves collecting and annotating a dataset of 193 intraoral periapical radiographs. The problem is formulated as both an object detection and keypoint detection task, enabling the precise identification of dental structures and clinically relevant landmarks, such as cemento-enamel junction (CEJ), current bone level (BL), and root level (RL). Additionally, we aim to detect periodontal disease-related conditions such as detached periodontal ligament space, furcation involvement, and alveolar ridge resorption. These detected keypoints and conditions, combined with tooth orientation, facilitate the automatic calculation of localised bone loss percentages, aiding in the accurate staging

of periodontal disease. We select YOLOv8 [5], a pose/keypoint detection, object detection and instance segmentation model, as the baseline model for this paper.

We adopt the YOLOv8 architecture [5] as the baseline model, leveraging its capabilities in pose estimation, object detection, and instance segmentation. Specifically, we fine-tune YOLOv8-pose to detect key dental landmarks and conditions, and pre-train YOLOv8-seg on a separate auxiliary dataset to segment teeth within the radiographs. The predicted segmentation masks are then utilised for post-processing to refine keypoint placement by aligning them to the outer tooth boundary, improving keypoint accuracy. Our experimental findings demonstrate that the model effectively identifies key anatomical landmarks, with post-processing contributing to increased performance when initial predictions exhibit a certain level of accuracy. However, performance declines when the model-generated keypoints or tooth segmentations are of poor quality. This research indicates the transformative potential of machine learning in dental diagnostics, paving the way for more accessible and efficient tools to improve patient outcomes in periodontal health.

2. Related Work

Advancements in machine learning have significantly contributed to the field of medical imaging and diagnostics [6, 7, 8], enabling automation and improving the accuracy of disease diagnosis [9, 10, 11, 12, 13, 14]. Object detection and keypoint detection models, in particular, have demonstrated considerable promise in medical applications, including the identification of tumors in radiographic images and the detection of anomalies in ultrasound scans [15]. The integration of these technologies into periodontal bone loss detection has the potential to improve diagnostics by providing faster, more consistent, and widely accessible assessments.

Object detection involves the localisation and classification of objects within an image, indicated by bounding boxes over the detected objects. Object detection is primarily achieved using two-stage or single-stage detectors. Two-stage detectors use both a pre-trained region proposal network, to recommend features and initial bounding boxes, and a fully connected neural network to refine the recommended bounding boxes over the objects of interest. Single-stage detectors, such as You Only Look Once (YOLO) [16], expresses the problem as a regression task, enabling real-time performance by regressing pre-placed bounding box anchors typically using a convolutional

neural network (CNN). However, object detection still cannot provide the highly localised detections necessary for some medical imaging tasks, unlike segmentation and pose estimation models.

Keypoint detection, also referred to as pose estimation, focuses on predicting the precise (x, y) coordinates of relevant landmarks in an image. This task is similar to object detection but differs in that it predicts keypoints instead of bounding boxes. Keypoint detection methods generally fall into two categories: heatmap-based approaches [17, 18] and regression-based approaches [19, 20]. Heatmap-based methods utilise attention mechanisms to generate probability maps, highlighting key areas of interest for keypoint placement. Whereas, regression-based methods use pre-placed anchors that are directly regressed to the desired landmark location, similar to single-stage object detection models.

Instance segmentation models involve the detection of the pixel-level masks for each individual instance of an object within an image [21]. Unlike semantic segmentation, which assigns a single label to all pixels of the same class without distinguishing between separate instances, instance segmentation provides granular differentiation of overlapping structures. This capability is particularly beneficial in applications such as autonomous driving [22] and biomedical imaging [23, 24], where precise separation of individual objects is vital.

Within the dental domain, U-Net and other CNN based architectures [9] are now widely adopted for primarily segmentation tasks [25, 26] and other computer vision applications [27, 28] for detecting anatomical structures and pathological conditions. Attention-based models [29, 30] have also been explored for dental imaging tasks [31], but their reliance on large datasets poses a challenge in clinical settings.

Recent studies have investigated the automatic detection of periodontal disease using deep learning and signal processing techniques [29, 32]. Few methods utilise keypoint detection for periodontal assessment [33, 34, 35, 36]. Existing approaches predominantly focus on detecting cemento-enamel junctions, current bone levels, and root levels to estimate the percentage of bone loss [37, 38]. Additionally, research has explored the detection of alveolar bone defects through segmentation techniques [39] and the classification of horizontal and vertical bone loss [40]. However, existing keypoint periodontal detection methodologies do not combine all necessary defect detections to make an informed diagnosis via radiography. The detection of detached periodontal ligament space and alveolar bone resorption defects are not seen

in other works.

For our study, we selected YOLOv8 [5], a state-of-the-art single-stage object detection, keypoint detection, and instance segmentation model, known for its efficiency and accuracy. We utilised YOLOv8-pose for keypoint detection tasks and YOLOv8-seg for instance segmentation tasks. The YOLO [16] architecture has been widely adopted in various domains for its ability to perform real-time object detection [41]. Key architectural features include a decoupled head structure for enhanced multi-task learning, multi-scale feature extraction similar to Feature Pyramid Networks [42], and DETR-inspired attention mechanisms [43] to refine localisation in complex images with overlapping objects [30, 44].

3. Methodology

3.1. Dataset Annotation

The dataset consists of 193 periapical radiographs, collected from 193 patients representing a range of demographics and varying extents of periodontal health. A total of 582 teeth are included in the dataset, comprising 386 single-root teeth, 160 double-root teeth, and 34 triple-root teeth.

The collection of radiographs was carried out by one periodontist (NG) and one radiologist (MG), both with a minimum of 10 years of clinical experience. The evaluation of periodontal disease extent was conducted independently, without a time limit, and the evaluation periods were adjusted based on the availability of the observers. The annotators were tasked with classifying the area exhibiting the greatest bone loss into four categories: no bone loss, mild bone loss, moderate bone loss, and severe bone loss [45]. A consensus was reached between the two observers to assign the final category for each image.

We conducted comprehensive annotation of the collected radiographs, divided into four steps. These include annotating Bone Level Keypoints (BLK) for each tooth, identifying the Teeth Bounding Box (TBB) with tooth orientation, annotating Alveolar Ridge Resorption (ARR) keypoints, and detached Periodontal Ligament Space (PLS) bounding boxes. Figure 1 provides visual examples of the annotations.

Bone Level Keypoints (BLK)

The first step involves labelling keypoints relating to the Cementoenamel Junction (CEJ), current Bone Level (BL), and Root Level (RL) on both the mesial (-m) and distal (-d) sides of the teeth. For triple and single-root

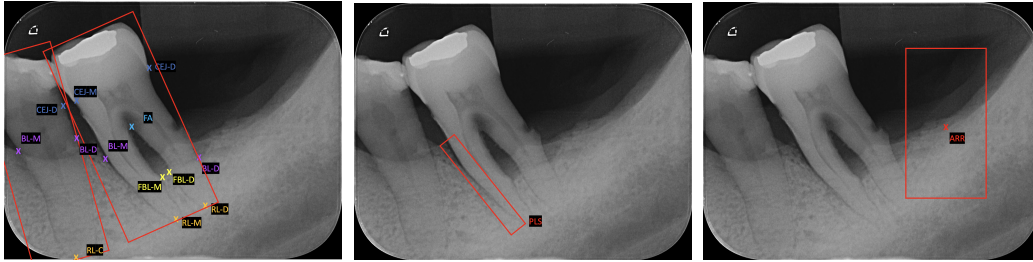


Figure 1: Three images containing example annotations of the collected keypoints and bounding boxes. **Left:** single root and double root tooth with example BLK and TBB annotations. **Middle:** double root tooth with example PLS bounding box. **Right:** missing tooth with example ARR keypoint and bounding box.

teeth, a central root level (RL-c) was also included, where single root teeth do not contain RL-m or RL-d keypoints. For multi-root teeth, additional keypoints were annotated to indicate furcation involvement. These included Furcation Apex (FA) and Furcation Bone Level mesial/distal (FBL-m, FBL-d), to indicate furcation involvement, and Furcation Bone Level Healthy (FBL-H) with FA, to indicate a healthy furcation area. FBL-h keypoints are not used by the model, but to identify indication of healthy furcation areas by the annotator, if furcation involvement keypoints are lost or missed in the annotation process. These annotations provide crucial information for assessing the extent of bone loss and periodontal disease, aligning the task with a computer vision problem.

Alveolar Ridge Resorption (ARR)

In the ARR annotation step, focus is placed on identifying the areas of Alveolar Ridge Resorption. This involves annotating the current bone level at locations where a tooth is missing and bone resorption has begun. Annotations for ARR are completed as a bounding box indicating the missing tooth area and a keypoint indicating the lowest point of ARR within the localised area of the missing tooth.

Periodontal Ligament Space (PLS)

In this step, areas where the periodontal ligament space had detached were annotated. PLS annotations in this category indicate ligament spaces that have detached from the tooth with a rotating bounding box, serving as indicators of compromised periodontal health rather than a healthy ligament space.

Teeth Bounding Box (TBB)

The final step in the annotation process involved annotating rotating bounding boxes around each tooth. These serve as a reference box for the model detections of BLK locations and facilitates the calculation of bone loss percentages by identifying tooth orientation.

3.1.1. Annotation Cleaning and Processing

Once the annotations were completed, the dataset underwent a cleaning process to prepare it for training. Some annotations, such as ARR keypoints and bounding boxes for certain teeth, were either missing or misclassified. In addition, keypoints were not initially linked to their corresponding bounding boxes. To address these issues, keypoints were automatically matched to their bounding boxes by measuring the horizontal distance between each keypoint and the center of the each bounding box, choosing the shortest distance for each keypoint class. In cases where automatic matching failed, manual adjustments were made to correctly assign keypoints.

Figure 2 presents the instance counts for each bounding box and keypoint class after cleaning. Figure 2a displays the counts for bounding boxes, and Figure 2b presents the keypoint counts. Some keypoint classes, such as Triple Root boxes, ARR boxes, FBL-m, and FBL-d keypoints, had low instance counts, which could pose challenges related to model overfitting.

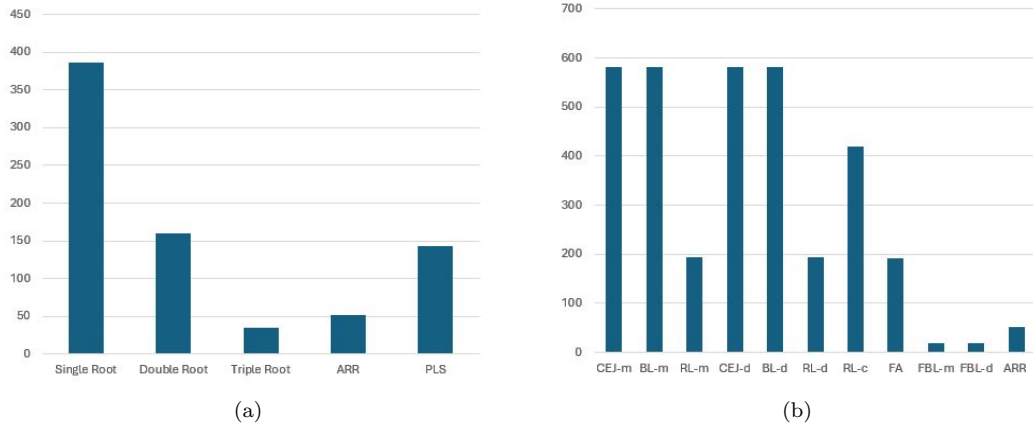


Figure 2: (a): Bar plot showing the counts of bounding box class instances of our baseline dataset before processing and after cleaning. (b): Bar plot showing the counts of keypoint instances of our baseline dataset before processing and after cleaning.

Given the limitations of current pose estimation models, which do not support rotation indices for bounding boxes, we removed the rotational com-

ponent from the TBB and PLS bounding boxes. However, if deployed in real world scenarios, a method of tooth orientation detection is required.

To ensure compatibility with the YOLOv8-pose model, which requires all keypoints to be detected with visibility identifiers with assignment to a bounding box, we formatted the data into five bounding box classes: 'Single Root', 'Double Root', 'Triple Root', 'ARR', and 'PLS'. Each keypoint for each box class was assigned a visibility value as follows: visibility 0 (not visible, not trained), visibility 1 (partially visible, trained), and visibility 2 (visible, trained). A summary of the visibility assignment for each keypoint depending on their attached bounding box class is shown in Table 1.

	CEJ-m	BL-m	RL-m	CEJ-d	BL-d	RL-d	RL-c	FA	FBL-m	FBL-d	ARR
Single Root	2	2	0	2	2	0	2	0	0	0	0
Double Root	2	2	2	2	2	2	0	2	2 or 1	2 or 1	0
Triple Root	2	2	2	2	2	2	2	2	2 or 1	2 or 1	0
ARR	0	0	0	0	0	0	0	0	0	0	2
PLS	0	0	0	0	0	0	0	0	0	0	0

Table 1: Table displaying the visibility setting for each keypoint relating to each bounding box class. 0: Not Visible and Not Trained, 1: Partially Visible and Trained, 2: Visible and Trained.

CEJ and BL keypoints are present for all three of the tooth bounding boxes, with varying RL keypoints depending on the number of roots present in the tooth. For furcation involvement, healthy furcation areas were processed to include both FBL-m and FBL-d keypoints at the same location as the Furcation Apex (FA) keypoint, with visibility 1, ensuring the model could be trained on all instances, regardless of whether the furcation area was diseased. ARR keypoints are given their own ARR bounding box with ARR being the only keypoint trained. Additionally, no keypoints were used for the detection of PLS objects, as it is solely based on bounding box detection.

After completing the annotation and preprocessing steps, the final dataset consists of 193 images, 582 tooth bounding boxes, and a total of 3520 keypoints. Prior to processing, the dataset included 19 FBL-m and 19 FBL-d keypoints indicating furcation involvement. However, after incorporating FBL keypoints for healthy furcation areas, the dataset now contains 191 instances of both FBL-m and FBL-d keypoints.

3.2. Heuristic Post-Processing

The most of the periodontal bone loss related keypoints that are required to calculate localised percentage of bone loss, must exist on the edge of the

nearest tooth. This is because the percentage of bone loss is determined relatively to the length of the nearest tooth’s root. If the pose detection model fails to predict the exact location of the keypoints, particularly when the predictions are detached from the edge of the affected tooth, we can post-process the keypoints to realign to the edge of the tooth, improving keypoint predictions.

We propose a heuristic based post-processing module, that leverages prior anatomical knowledge and an independently pre-trained tooth segmentation model, which has been trained on an auxiliary tooth identification dataset. The segmentation model determines the outline of each tooth in the image and the module adjusts the keypoint predictions to align along the edge of the relevant tooth.

The post-processing module uses the predicted segmentation masks and keypoints for a given image and matches each set of visible keypoints to the closest segmentation mask. The module achieves this by measuring the average Euclidean distance between each keypoint in a set of predicted keypoints and the closest edge pixel on the segmentation mask. The segmentation mask with the lowest average Euclidean distance to the set of visible keypoints is the matching mask. The module then replaces the visible predicted keypoint coordinates with the matching edge pixel coordinates. An example of this process can be seen in Figure 3.

3.3. Percentage of Relative Correct Keypoints Metric

We propose an evaluation metric, Percentage of Relative Correct Keypoints (PRCK), which is based on the Percentage of Detected Joints (PDJ) metric [46] for pose estimation. PDJ follows the same principle as NME, where a metric is adjusted to a normalising factor that grounds the metric to the relative scale of the objects in the image. PDJ and PRCK calculates the percentage of correct predicted keypoints in the dataset, if the predicted keypoint is within a specified threshold of the normalising factor to the target keypoint, meaning the higher the metric the better the performance. Both metrics have similar equations, but the normalising factor L for PDJ is the current bounding box diagonal distance for a given keypoint, while PRCK uses the average bounding box diagonal distance of all boxes in the image.

PDJ works as a metric for human pose detection, as target human keypoints compress in distance to each other as the human faces laterally to the camera, so metrics should penalise incorrect predicted keypoints for lateral facing humans (shorter bounding box diagonal) more than anterior facing

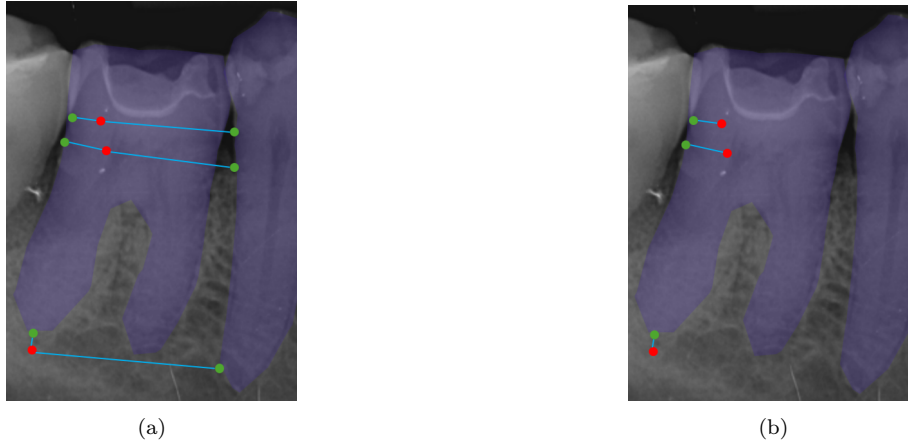


Figure 3: Drawn example of how the post-processing module matches keypoints to segmentation masks. Images only show distal CEJ, BL and RL keypoints, with predicted keypoints (red) and the closest segmentation mask edge pixel (green) for two example segmentation masks (purple). (a) depicts the closest edge pixel for the two segmentation masks. (b) depicts the chosen edge pixels by the module as it has the lowest average distance.

humans (larger bounding box diagonal). However, this does not work for our domain, as we potentially have three different tooth sizes in the same image which would unfairly penalise single root teeth over multi-root teeth. We use the average box diagonal distance for PRCK, which grounds the metric to the relative size of the objects in a given image, while also standardising the thresholds for all tooth objects in the image. The PRCK metric is expressed in Equation (1).

$$\text{PRCK} = \frac{1}{n} \sum_{i=1}^n \text{bool}(\|y_i - \hat{y}_i\|_2^2 < d_{\text{thresh}} \cdot L), \quad (1)$$

where `bool` is a function that returns 1 if the condition is true and 0 if false and d_{thresh} is a specified threshold value between 0 and 1 as a fraction of the normalising factor. The normalising factor L is the same as with NME.

3.4. YOLOv8 for Alveolar Bone Loss and Tooth Segmentation

Inspired by YOLO-pose results for human pose estimation on the COCO dataset [47], we utilise YOLOv8-pose for bone loss keypoint detection as the problem statement is similar to human pose estimation. We also utilise

YOLOv8-seg to perform instance segmentation, trained on a separate auxiliary dataset to support binary class tooth segmentation. The YOLOv8-pose and YOLOv8-seg model are trained in a supervised setting which takes input as image $\mathbf{x}_i \in \mathbb{R}^{h \times w \times c}$, and outputs the predicted bounding boxes and keypoints in Equation (2) for YOLOv8-pose and the predicted segmentation masks in Equation (3) for YOLOv8-seg, where $h \times w \times c$ is the image, is the height, width, and channel, respectively.

$$\bar{y}_{i_kpt} = \{class, C_x, C_y, W, H, box_{conf}, class_{conf}, K_x^1, K_y^1, K_{conf}^1, K_x^2, K_y^2, K_{conf}^2, \dots, K_x^n, K_y^n, K_{conf}^n\} \quad (2)$$

$$\bar{y}_{i_seg} = \{class, C_x, C_y, W, H, box_{conf}, class_{conf}, C_{(x_1, y_1)}, C_{(x_2, y_1)}, \dots, C_{(x_1, y_2)}, C_{(x_2, y_2)}, \dots, C_{(x_{imgw}, y_{img_h})}\} \quad (3)$$

where \bar{y}_{i_kpt} is the pose detection outputs for a single object, *class* is the bounding box class, C_x, C_y are the bounding box centre coordinates, W, H are the width and height of the box, box_{conf} is the bounding box confidence, $class_{conf}$ is the bounding box class confidence, K_x, K_y are the keypoint coordinates for each keypoint class attached to a bounding box, and K_{conf}^n is the keypoint confidence, \bar{y}_{i_seg} is the instance segmentation detection outputs for a single object, $C_{(x,y)}$ is the class of a specified pixel in the target image.

4. Experiments and Results

4.1. Experimental Setup

4.1.1. Metrics

We evaluate the performance of the model on our dataset under two main sections, pose detection metrics and localised disease classification metrics. Pose detection metrics are comprised of standard bounding box and adapted pose detection metrics, while the disease classification metrics evaluate the bone loss stage classifications calculated for each tooth for mesial and distal sides.

Keypoint and Bounding Box Metrics

For the evaluation of bounding box performance, we employed mean Average Precision (mAP), calculated at two different Intersection over Union

(IoU) thresholds: 0.5 and 0.5:0.95. mAP at 0.5 IoU threshold evaluates the performance of bounding box detection when considering a significant overlap between the predicted and ground truth bounding boxes. However, mAP at 0.5:0.95 IoU range assesses the model’s performance across a spectrum of IoU thresholds, providing insights into its robustness under various detection scenarios. Higher mAP values indicate better overall performance in object detection. We also evaluate the performance using Precision and Recall, where precision measures the accuracy of positive detections, while Recall assesses completeness.

We evaluate the keypoint performance using two primary metrics, Normalised Mean Error (NME) and our proposed PRCK. NME is a metric that evaluates the error comparing the distance of the predicted and target keypoint positions, relative to a normalising factor that adjusts the effect of the metric based on a value that grounds the distances to the specific image. NME is an error measure, meaning the lower the value the better the performance. NME is expressed as $NME = \frac{1}{n} \sum_{i=1}^n \frac{\|y_i - \hat{y}_i\|_2}{L}$, where n is the total number of keypoints for a given class, y_i is the target keypoint, \hat{y}_i is the predicted keypoint, L is the normalising factor, $\|y_i - \hat{y}_i\|_2$ and is the Euclidean Distance of y_i and \hat{y}_i . We define the normalising factor as the average diagonal distance of all tooth bounding boxes in the image. We evaluate PRCK at three thresholds, 0.5, 0.25, and 0.05 of the normalising factor.

Disease Classification Metrics

To evaluate the models ability to detect the correct disease stages of periodontal disease, we employ another set of metrics that compare the classification performance for conditions necessary to diagnosis periodontal disease stages.

To facilitate these metrics, we calculate the Percentage of Bone Loss (PBL) using the CEJ, BL, and RL keypoints, for the distal and mesial sides, for each annotated tooth in the image. The BL and RL keypoints are extrapolated to a straight line originating from the CEJ at the angle specified by the original target rotating bounding box angle. We calculate the percentage of bone loss as $PBL = \frac{\|CEJ-BL\|_2}{\|CEJ-RL\|_2}$, where $\|CEJ - BL\|_2$ is the Euclidean distance of the CEJ and BL, and $\|CEJ - RL\|_2$ is the Euclidean distance of the CEJ and RL. PBL is calculated for each root in the current tooth individually, with the highest PBL being chosen as the true value, as percentage of bone loss in clinical practice is measured from the shortest root. With the

percentage of bone loss being calculated for all target teeth in the image for distal and mesial sides for both target and predicted keypoints, we can generate a confusion matrix for each disease stage classification as $PBL < 0.15$, $0.15 \leq PBL < 0.33$, $0.33 \leq PBL < 0.66$ and $PBL \geq 0.66$, as Healthy, Mild, Moderate, Severe, respectively. While clinical PBL measurements are taken from CEJ-2mm, we cannot determine the exact position of the healthy bone level due to the anonymous nature of the dataset, the unknown x-ray receptor holder dimensions, and no software fixing of foreshortening/elongation artefacts.

Additionally, we facilitate furcation involvement classification metrics by measuring the Euclidean distance of the each FBL keypoints to the FA keypoint. If any one of the FBL keypoints has an Euclidean distance greater than 0.05 of the average diagonal distance for all bounding boxes in the image, it is considered to have furcation involvement. A confusion matrix can be calculated using the furcation involvement classification for the pred and target data.

Using the confusion matrix for these two classifications, we calculate the precision, recall/sensitivity, dice coefficient/F1 score and specificity. We do not include accuracy in our metrics, as the training of a deep learning pose estimation model requires a large number of images with unknown number and varying amounts of objects in the image. The accuracy metric is highly dependent on true negative samples and the balancing of positive and negative samples within the target dataset. If there are a high number of negative samples in the dataset when comparing predicted against target results, it can unfairly boost metrics with True Negative in the numerator. Since balancing the instances of each disease stage is nearly impossible to do without 'cherry-picking' specific samples, due to the local nature of periodontal disease within the same image, we mainly focus on prevalence invariant metrics. Following the same reasoning as above, results for the specificity metric should be looked at sceptically.

4.1.2. Training

We fine-tuned the YOLOv8-pose model using pre-trained weights trained on the COCO dataset. We fine tuned the model using a starting learning rate of 0.001 that is lowered by 0.001 if the loss does not improve for 3 epochs. All images are resized to 640×640 for training and evaluation purposes. Before we split the dataset into train and validation sets, we removed a holdout test set of 18 images. On the remaining 175 images, we trained 5 models

with the same parameters using 5 fold cross validation to train and evaluate each model on an alternating 80 : 20% 140 : 35 image train:val splits, so we could calculate the average and standard deviation performance across all data samples in the train/val sets. Holdout test set results are seen in 5.

4.1.3. Post-Processing

To enable heuristic post-processing we need to find the edges of each independent tooth in the image. We fine-tuned YOLOv8-seg on the open-source panoramic radiograph auxiliary dataset [48], to only be used in the inference stage of our separate domain periapical radiograph dataset. The panoramic auxiliary dataset consists of 598 images annotated by 15 trainees from the Democratic Republic of Congo, with the images originating from patients of varying ages from Paraguay [49]. The panoramic radiograph dataset and our periapical dataset are from different sources, patients and radiography techniques.

Due to the auxiliary dataset containing panoramic radiographs only, we pre-processed the dataset to manually crop the images into six sub-images that partially resemble the crop of periapical radiographs. We cropped each image to contain the left posterior teeth, right posterior teeth, and anterior teeth, for both the maxillary and mandibular rows, with slight random variation to the position, width and height of the crop. This gave us 3,588 images for training and validation. We also processed the dataset to reduce the 32 classes of each possible tooth number into a single class 'tooth'. We split the images into a 3230 : 358, 90 : 10% train:val sets.

As the trained segmentation model is to be used on our differing domain periapical dataset, which does not contain its own tooth segmentation labels, we evaluated the performance of the segmentation model qualitatively on our dataset.

We trained the model for 20 epochs, selecting the best performing epoch on the validation set as the final model. We intentionally slightly underfit the model, so it would have improved generalisability on our dataset of a differing domain and distribution.

The post-processing module is not used on any of the furcation related keypoints (FA, FBL-m, FBL-d) or the alveolar ridge resorption (ARR) keypoint. This was done as there are significant instances of overlapping roots in some double and triple root teeth, which makes the segmentation of the furcation area impossible, causing the post-processing to fail for these examples. Additionally, ARR keypoints indicate bone resorption in areas with

missing teeth, so there are no nearby teeth to adjust the keypoint to.

4.2. Results

4.2.1. Quantitative Results

Tables 2 and 3 reports the YOLOv8-pose nano validation evaluation metrics for bounding boxes and keypoints, respectively. Table 3, compares the validation performance between YOLOv8-pose nano with and without post-processing. Bounding box metrics include mAP at IoU threshold 0.5 and 0.5-0.95, precision and recall. Keypoint metrics include Percentage of Relative Correct Keypoints at normalising factor threshold 0.5, 0.25 and 0.05, and Normalised Mean Error. Metrics are displayed as average folds and (standard deviation) over all folds for all bounding box and keypoint classes, with the average over all classes.

Metrics	Bounding Box Class					
	Single Root	Double Root	Triple Root	ARR	PLS	Average
mAP^{0.5}	0.928 (±0.025)	0.966 (±0.017)	0.839 (±0.080)	0.678 (±0.026)	0.163 (±0.014)	0.715 (±0.296)
mAP^{0.5-0.95}	0.670 (±0.030)	0.755 (±0.032)	0.622 (±0.099)	0.317 (±0.031)	0.060 (±0.009)	0.485 (±0.264)
Precision	0.836 (±0.052)	0.927 (±0.038)	0.632 (±0.112)	0.647 (±0.075)	0.242 (±0.042)	0.657 (±0.246)
Recall	0.913 (±0.051)	0.881 (±0.065)	0.875 (±0.155)	0.654 (±0.079)	0.151 (±0.060)	0.695 (±0.301)

Table 2: Bounding box validation metrics for YOLOv8-pose nano model on our dataset.

Performance for the bounding box metrics for single, double and triple root are high with low deviation in performance over 5 folds. ARR boxes have a dip in performance, especially for mAP 0.5-0.95, which shows an inaccuracy at precisely detecting the bounding box. This is likely due to the small number of samples, but keypoint metrics are the primary identifier of performance for ARR detection. PLS performance is extremely low for all metrics, which is likely due to the small number of instances in the dataset or low sample rate of the condition in patients. However, as the bounding box instances for PLS are at 142 with ARR instances being at 52, this implies that the model cannot accurately differentiate between detached periodontal ligament space and healthy periodontal ligament space in this low data regime.

Metrics	Classes Without Post-Processing											
	CEJ-m	BL-m	RL-m	CEJ-d	BL-d	RL-d	RL-c	FA	FBL-m	FBL-d	ARR	Average
PRCK ^{0.5}	0.830 (±0.024)	0.929 (±0.018)	0.826 (±0.115)	0.981 (±0.011)	0.982 (±0.007)	0.812 (±0.173)	0.858 (±0.018)	0.921 (±0.060)	0.898 (±0.065)	0.877 (±0.074)	0.938 (±0.081)	0.901 (±0.034)
PRCK ^{0.25}	0.619 (±0.033)	0.707 (±0.062)	0.765 (±0.098)	0.747 (±0.054)	0.748 (±0.056)	0.719 (±0.176)	0.846 (±0.030)	0.916 (±0.060)	0.888 (±0.075)	0.872 (±0.073)	0.938 (±0.081)	0.752 (±0.045)
PRCK ^{0.05}	0.274 (±0.053)	0.299 (±0.066)	0.262 (±0.103)	0.337 (±0.070)	0.284 (±0.037)	0.174 (±0.115)	0.492 (±0.085)	0.652 (±0.149)	0.609 (±0.165)	0.575 (±0.151)	0.678 (±0.198)	0.360 (±0.063)
NME	0.289 (±0.022)	0.202 (±0.028)	0.307 (±0.128)	0.165 (±0.018)	0.167 (±0.016)	0.351 (±0.195)	0.208 (±0.020)	0.135 (±0.087)	0.167 (±0.098)	0.200 (±0.106)	0.133 (±0.127)	0.211 (±0.068)
Metrics	Classes With Post-Processing											
	CEJ-m	BL-m	RL-m	CEJ-d	BL-d	RL-d	RL-c	FA	FBL-m	FBL-d	ARR	Average
PRCK ^{0.5}	0.823 (±0.023)	0.934 (±0.023)	0.821 (±0.112)	0.949 (±0.013)	0.972 (±0.013)	0.812 (±0.173)	0.844 (±0.008)	-	-	-	-	0.893 (±0.033)
PRCK ^{0.25}	0.580 (±0.031)	0.701 (±0.059)	0.746 (±0.102)	0.675 (±0.059)	0.732 (±0.058)	0.685 (±0.181)	0.826 (±0.021)	-	-	-	-	0.726 (±0.045)
PRCK ^{0.05}	0.336 (±0.031)	0.355 (±0.049)	0.238 (±0.075)	0.405 (±0.047)	0.340 (±0.017)	0.201 (±0.151)	0.521 (±0.075)	-	-	-	-	0.401 (±0.050)
NME	0.297 (±0.022)	0.201 (±0.027)	0.318 (±0.125)	0.171 (±0.021)	0.168 (±0.016)	0.354 (±0.197)	0.228 (±0.021)	-	-	-	-	0.216 (±0.067)

Table 3: Keypoint validation metrics for YOLOv8-pose nano model with and without post-processing on our dataset. Metrics in bold indicate the better performing method.

For the baseline model without post-processing, All keypoint classes perform well at predicting the general area of the target keypoints according to PRCK 0.5 and 0.25 metrics. However, most metrics have diminished but relatively promising results for PRCK 0.05. Root level keypoint RL-d has a PRCK 0.05 of 0.174, which implies that the baseline model performs poorly at precisely locating the exact apex of the distal roots. All furcation and ARR keypoints have the most consistent and highest performing metrics out of all keypoints. However, due to the setup of the furcation keypoints, the performance of these keypoints does not indicate if the model correctly identifies furcation involvement, leaving the evaluation of this to the disease classification metrics in Table 4 and Table 5.

For the model with post-processing, effected keypoint classes exhibit a small reduction in performance for PRCK 0.5, PRCK 0.25, and NME metrics, when compared to the model without post-processing, but exhibit an increased PRCK 0.05 metric, excluding RL-m. This implies that the post-processing improves the keypoint location by small amounts for the majority of samples, causing an increased performance in PRCK 0.05, but for a small number of samples the post-processing fails, causing a worse PRCK 0.5 and 0.25 performance.

Metrics	Percent of Bone Loss Classes Without Post-Processing									
	Healthy Mesial	Mild Mesial	Moderate Mesial	Severe Mesial	Average Mesial	Healthy Distal	Mild Distal	Moderate Distal	Severe Distal	Average Distal
Precision	0.801 (±0.046)	0.510 (±0.030)	0.597 (±0.201)	0.000 (±0.000)	0.636 (±0.057)	0.725 (±0.051)	0.546 (±0.052)	0.566 (±0.113)	0.000 (±0.000)	0.612 (±0.059)
Recall	0.715 (±0.095)	0.671 (±0.070)	0.329 (±0.140)	0.000 (±0.000)	0.572 (±0.034)	0.756 (±0.085)	0.623 (±0.081)	0.291 (±0.108)	0.000 (±0.000)	0.557 (±0.037)
Dice	0.752 (±0.056)	0.576 (±0.011)	0.405 (±0.147)	0.000 (±0.000)	0.577 (±0.042)	0.739 (±0.066)	0.581 (±0.062)	0.370 (±0.091)	0.000 (±0.000)	0.564 (±0.038)
Specificity	0.778 (±0.066)	0.684 (±0.063)	0.970 (±0.027)	0.993 (±0.011)	0.856 (±0.011)	0.738 (±0.027)	0.699 (±0.049)	0.963 (±0.020)	0.991 (±0.014)	0.848 (±0.022)

Metrics	Percent of Bone Loss Classes With Post-Processing									
	Healthy Mesial	Mild Mesial	Moderate Mesial	Severe Mesial	Average Mesial	Healthy Distal	Mild Distal	Moderate Distal	Severe Distal	Average Distal
Precision	0.801 (±0.052)	0.534 (±0.053)	0.581 (±0.201)	0.000 (±0.000)	0.638 (±0.049)	0.725 (±0.054)	0.532 (±0.057)	0.506 (±0.174)	0.000 (±0.000)	0.588 (±0.077)
Recall	0.723 (±0.083)	0.686 (±0.061)	0.354 (±0.110)	0.000 (±0.000)	0.587 (±0.028)	0.753 (±0.083)	0.600 (±0.088)	0.288 (±0.122)	0.000 (±0.000)	0.547 (±0.044)
Dice	0.757 (±0.058)	0.596 (±0.029)	0.424 (±0.114)	0.000 (±0.000)	0.593 (±0.033)	0.738 (±0.066)	0.562 (±0.065)	0.354 (±0.119)	0.000 (±0.000)	0.552 (±0.051)
Specificity	0.778 (±0.058)	0.705 (±0.062)	0.965 (±0.022)	0.995 (±0.007)	0.861 (±0.014)	0.737 (±0.042)	0.693 (±0.051)	0.953 (±0.025)	0.991 (±0.014)	0.844 (±0.023)

Table 4: Disease classification validation metrics for YOLOv8-pose nano model on our dataset. Metrics in bold indicate the better performing method.

Class	Furcation Involvement Metrics			
	Precision	Recall	Dice	Specificity
All	0.248 (±0.089)	0.333 (±0.136)	0.280 (±0.098)	0.865 (±0.049)

Table 5: Furcation involvement classification validation metrics for YOLOv8-pose nano model on our dataset.

Within Table 4 and Table 5 we report the YOLOv8-pose nano validation disease classification metrics for percentage of bone loss stages and furcation involvement, respectively, for the YOLOv8-pose nano model. Table 4 also compares the performance of the model with and without post-processing. Metrics are displayed as precision, recall, dice, and specificity for both evaluations, as the average metric and (standard deviation) over all folds.

PBL classification metrics without post-processing shows consistent performance over both mesial and distal sides of the teeth for individual disease

classes. We see excellent performance for the healthy class, but slightly worse performance for each step up in disease severity. The severe disease stage registers as 0.0 for precision, recall, and dice, as no True Positive values were recorded, which is due to the very low number of severe samples in the dataset. The performance of the model with post-processing shows a slight increase in performance for mesial PBL metrics, but a slight decrease in performance for distal side PBL metrics, which implies the post-processing module positively effects mesial keypoints more than distal keypoints.

Furcation involvement classification metrics show poor performance, which in conjunction with the high performance for the keypoints, indicates either poor performance by the model at detecting furcation involvement or the number of instances at 19 being too low to accurately evaluate the model’s ability to detect furcation involvement.

4.2.2. Qualitative Results

Viewing the model predictions without post-processing qualitatively, we can see that the majority of keypoint predictions are close to their respective target keypoints. However, in Figure 4a, we can see poor performance at detecting PLS bounding boxes with both false positive and false negative predictions. Additionally, we can see the model occasionally predicts edge teeth that were not labeled due to the lack of information in the radiograph for that tooth, the keypoints for these cases are usually very poor due to the lack of information in the image and low training samples for these cases. We also see that in some cases where the third molar is close to the second molar, it can confuse the model as to the true location of the keypoints directly next to the third molar. We can also see how the model predicts furcation keypoints, where they are predicted close to the apex, with all three keypoints having close spread to each other when indicating a healthy furcation area.

In Figure 4b the predicted keypoints are closer to their respective target keypoints. However, we can see a recurring problem also seen in Figure 4b and other radiographs, where keypoints are predicted at the correct relative vertical position to the tooth, but are well within or away from the edge of the tooth along the horizontal axis. We also see in Figure 4b the models ability to accurately detect ARR keypoints and bounding boxes, but there still are some examples where the model predicts false positive ARR keypoints when there is no resorption occurring.

When viewing the model predictions with post-processing qualitatively,

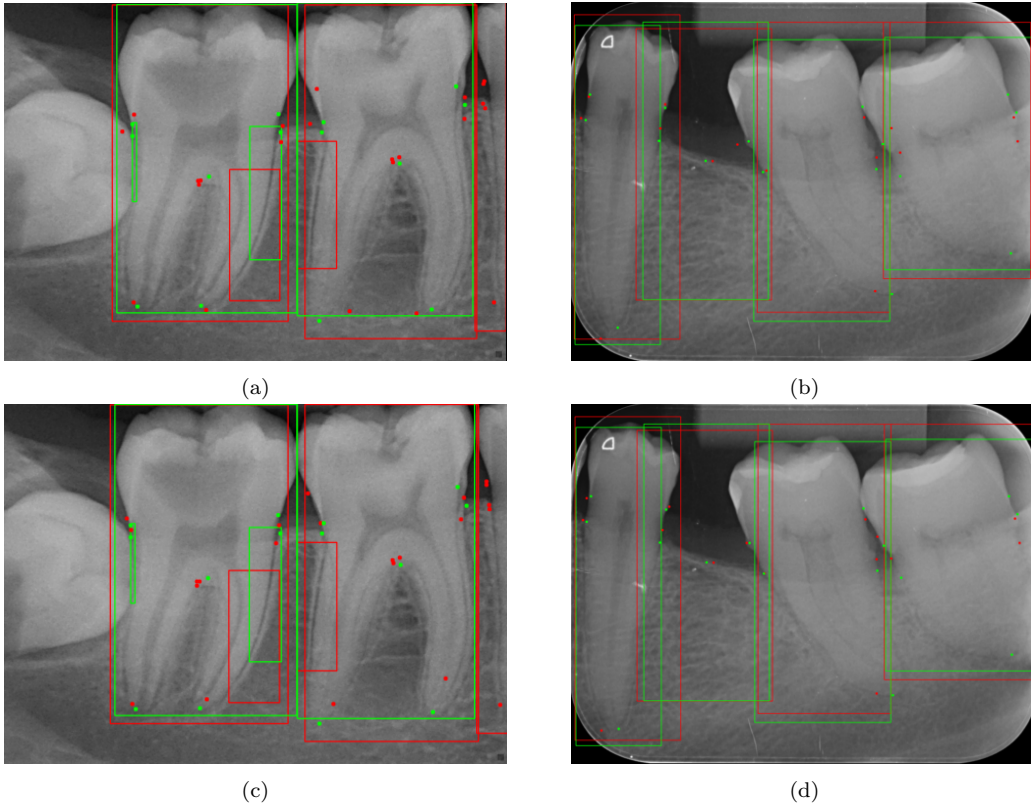


Figure 4: Images depicting predicted (red) and target (green) results from YOLOv8-pose nano on our proposed validation dataset. Images (a) and (b) are without post-processing, (c) and (d) are with post-processing

we can see a general improvement in keypoint locations compared to the model without post-processing. Figure 5a depicts how the post-processing module affects the majority of incorrect keypoint predictions by the model. The post-processing module appears to adjust keypoints to their correct location when the model predicts keypoints in impossible locations such as keypoints that are detached from the edge of the effected tooth. However, as seen in Figure 5b, there are edge cases where the keypoints predictions or predicted segmentation masks are so poor that the post-processing module fails and moves the keypoints further away from the target location. Additionally, in Figure 4c and Figure 4d, we can see the post-processing module both improve incorrect keypoints for CEJ and BL keypoints, and sometimes incorrectly move keypoints due to inaccurate predicted segmentation masks in RL keypoints.

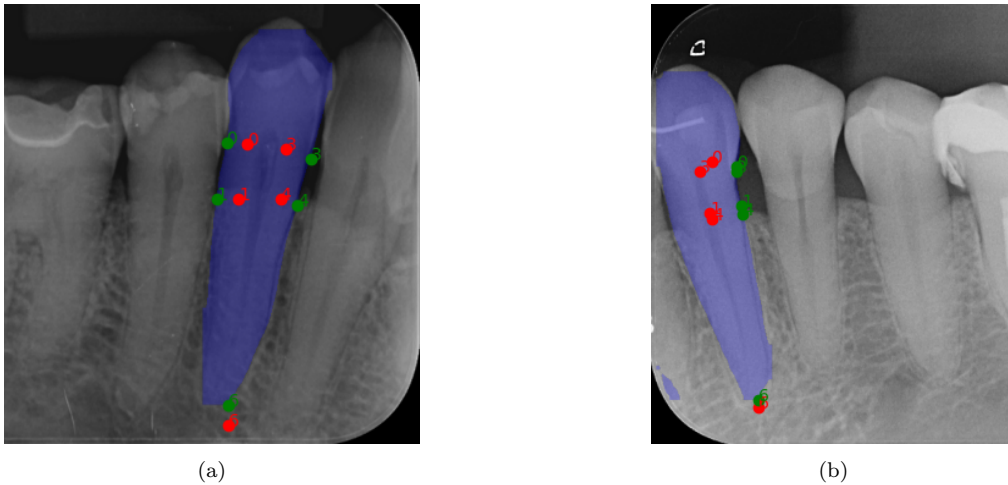


Figure 5: Two images containing non post-processed predicted keypoints (red), post-processed predicted keypoints (green) and predicted segmentation masks (blue) results from YOLOv8-pose/seg nano on our proposed validation dataset.

4.3. Discussion

Periodontal disease treatment is based on an accurate classification of the disease to achieve an adequate diagnosis, prognosis, and treatment plan that minimise possible human errors. The diagnosis of periodontal disease is made through clinical and radiographic analysis, which can be subjective in some cases. The development of artificial intelligence tools could assist

clinicians in optimising care for each patient. Advances in artificial intelligence are increasing due to the increased digitisation of radiography (and healthcare in general), the development of novel algorithms and neural network architectures, and the increasing computational power available. The advantage is that periodontists would not have to manually calculate the bone loss percentage for each tooth, a very time-consuming and sometimes inaccurate process.

Recently, deep learning has been applied in periodontics as an innovative model for diagnosing periodontal bone loss and the stage of periodontitis using panoramic radiographs [50, 51, 52, 53] and periapical radiographs [54, 55, 32, 56, 57, 58], demonstrating a variable accuracy rate from 0.41 to 0.889. However, Krois et al. [51] obtained higher accuracies when compared to the reported accuracies of pretrained CNNs (AUC values of 0.94–0.95). Moran et al. [58] used periapical radiographs and tested the performance of CNN models. The study indicated high accuracy, precision, recall, specificity, and negative predictive values: 0.817, 0.762, 0.923, 0.711, and 0.902, respectively and could be used in bone loss determination. In the present study, our model was comparable at detecting bounding boxes and is able to locate the relevant keypoints used in detecting periodontal bone loss using.

The use of periapical radiographs instead of manually cropped image segments from panoramic radiographs can improve the model detection, periapical radiographs subsets were easier to assess due to a strict inclusion criterion with good image projection and quality contrast. Outcomes difference in panoramic radiographs investigations is due to the technique being more sensitive to patient movements and positions than intraoral radiographs. All these variations can be explained in the sample, as well as the preferred architectures used. Also, some studies select distinct techniques, like classification, object detection, or segmentation, to conduct image processing. Therefore, it is not feasible to make direct comparisons between success rates obtained from various studies. Our sample had a homogeneous distribution of images, based on the severity of bone loss. This may have contributed to the augmentation of the diagnostic accuracy values. Future studies should investigate the impact of factors like image projection or quality contrast on the assessment ability to improve the model performance.

The data annotation method of using keypoints to detect periodontal bone loss, allows for stage agnostic detection and increases annotation counts. Detecting periodontal disease stages only using a stage-dependent method such as object detection, would cause poor performance with disease stage

classes with small instance counts and with the highly imbalanced instances of periodontal disease stages in the dataset we would see poor performance for said classes. Additionally, the method of detection provides a clear and easily understood method for clinicians, as it automates a process that is already performed manually. The method also allows for easy identification and correction of false predictions, as incorrect keypoint locations can be easily moved to the correct location if deployed in the real world.

A limitation of the present study is the complexity of making a complete diagnosis and prediction of periodontal disease using only two-dimensional periapical radiographs. For a more accurate diagnosis and prediction, it is necessary to thoroughly review the clinical and radiographic data together, including the patient’s history, clinical depth on probing, clinical attachment loss, bleeding on probing, and tooth mobility. Oral radiologists are highly qualified professionals, so any tool that can maximise the quality and efficiency of this process is of great interest. Artificial intelligence can also improve image quality by enhancing image reconstruction and filtering equipment, such as volumetric computed tomography, [59] potentially improving spatial resolution. Therefore, an algorithm using only periapical radiographic images does not provide sufficient evidence, though it can still serve as a reference for diagnosis. In this sense, developing a three-dimensional deep CNN algorithm for CBCT scans could be more useful and effective for diagnosis. Additionally, limitations persist within the model itself and dataset used. The small size of the dataset means that there is concern on the generalisability of the model, with specific concern with the poor performance at detecting severe bone loss, PLS bounding boxes and positive furcation involvement.

Without post-processing, the predicted keypoints often appear in impossible locations, within the bounds of the tooth or far outside the bounds of the tooth, which we coin the ‘floating keypoint problem’. The addition of the post-processing module does improve certain keypoint predictions and partially solves the ‘floating keypoint problem’. However, the method does rely on a minimum level of performance for both the tooth segmentation and keypoint predictions, resulting in worse keypoints in some cases.

5. Conclusion

In this work we propose a novel dataset annotation methodology, for the detection of periodontal disease related keypoints and defects, with the

goal of supplying fast and accurate information for a clinician to make an informed diagnosis. We also propose a keypoint detection metric for dental imaging domains, Percentage of Relative Correct Keypoints, that is based on the Percentage of Detected Joints metric, but normalises the metric to the average tooth size of present teeth in the image. Lastly, we propose a post-processing technique that moves certain keypoint predictions to the edge of the related tooth. We trained an off the shelf algorithm, YOLOv8-pose nano to detect relevant keypoints and bounding boxes for the diagnosis of periodontal disease. Our method displays high performance at the detection of certain keypoint and bounding box classes, but still performs poorly at other tasks, due to the limitations of the model and low instances of said classes. In future work we plan to increase the number of samples in the dataset, develop an improved model for the detection of periodontal disease related keypoints and improve post-processing techniques.

References

- [1] M. F. Helmi, H. Huang, J. M. Goodson, H. Hasturk, M. Tavares, Z. S. Natto, Prevalence of periodontitis and alveolar bone loss in a patient population at harvard school of dental medicine, *BMC Oral Health* 19 (2019) 254. doi:10.1186/s12903-019-0925-z.
- [2] A. Jayakumar, S. Rohini, A. Naveen, A. Haritha, K. Reddy, Horizontal alveolar bone loss: A periodontal orphan, *Journal of Indian Society of Periodontology* 14 (2010) 181-185. doi:10.4103/0972-124X.75914.
- [3] K. Al Shayeb, W. Turner, D. Gillam, Periodontal probing: A review, *Primary Dental Journal* 3 (08 2014). doi:10.1308/205016814812736619.
- [4] Department of Health and Social Care, Welsh Government, Department of Health Northern Ireland, Public Health England, NHS England, NHS Improvement, Chapter 5: Periodontal diseases, <https://www.gov.uk/government/publications/delivering-better-oral-health-an-evidence-based-toolkit-for-prevention/chapter-5-periodontal-diseases>, updated 9 November 2021 (2021).
- [5] G. Jocher, A. Chaurasia, J. Qiu, Ultralytics yolov8. 2023 (accessed 16 october 2024).
URL <https://github.com/ultralytics/ultralytics>

- [6] R. R. John, I. Ackerley, R. L. Smith, J. Scuffham, A. Robinson, V. Prakash, M. Shastry, M. Halling-Brown, E. Lewis, P. Strouhal, K. Wells, Automatic labeling of glycolytic volumes in pet using deep texture analysis, IEEE Nuclear Science Symposium, Medical Imaging Conference and International Symposium on Room-Temperature Semiconductor Detectors (2023) 1-2doi:10.1109/NSSMICRTSD49126.2023.10338391.
- [7] Z. Wang, Z. Wu, D. Agarwal, J. Sun, Medclip: Contrastive learning from unpaired medical images and text, arXiv preprint (2022) .doi:10.48550/arXiv.2210.10163.
- [8] J. Wu, W. Ji, Y. Liu, H. Fu, M. Xu, Y. Xu, Y. Jin, Medical sam adapter: Adapting segment anything model for medical image segmentation, arXiv preprint (2023) .doi:10.48550/arXiv.2304.12620.
- [9] O. Ronneberger, P. Fischer, T. Brox, U-net: Convolutional networks for biomedical image segmentation, Medical image computing and computer-assisted intervention 9351 (2015) 234-241. doi:10.1007/978-3-319-24574-4_28.
- [10] J. M. J. Valanarasu, P. Oza, I. Hacihaliloglu, V. M. Patel, Medical transformer: Gated axial-attention for medical image segmentation, Medical image computing and computer assisted intervention 12901 (2021) 36-46. doi:10.1007/978-3-030-87193-2_4.
- [11] R. Banks, B. Rovira-Lastra, J. Martinez-Gomis, A. Chaurasia, Y. Li, H-fcbformer: Hierarchical fully convolutional branch transformer for occlusal contact segmentation with articulating paper, Medical Image Understanding and Analysis 14860 (2024) 72-86. doi:10.1007/978-3-031-66958-3_6.
- [12] C. Myles, I. H. Um, D. J. Harrison, D. Harris-Birtill, Leveraging foundation models for enhanced detection of colorectal cancer biomarkers in small datasets, Medical Image Understanding and Analysis 14859 (2024) 329-343. doi:10.1007/978-3-031-66955-2_23.
- [13] A. Jaamour, C. Myles, A. Patel, S. J. Chen, L. McMillan, D. Harris-Birtill, A divide and conquer approach to maximise deep learning mammography classification accuracies, Plos One 18 (5) (2023) e0280841. doi:10.1371/journal.pone.0280841.

- [14] A. Patra, J. Noble, Sequential anatomy localization in fetal echocardiography videos, arXiv preprint (2018) .doi:10.48550/arXiv.1810.11868.
- [15] G. Dhiman, S. Juneja, W. Viriyasitavat, H. Mohafez, M. Hadizadeh, M. A. Islam, I. El Bayoumy, K. Gulati, A novel machine-learning-based hybrid cnn model for tumor identification in medical image processing, Sustainability 14 (3) (2022) . doi:10.3390/su14031447.
- [16] J. Redmon, S. Divvala, R. Girshick, A. Farhadi, You only look once: Unified, real-time object detection, conference on computer vision and pattern recognition (2016) 779-788doi:10.1109/CVPR.2016.91.
- [17] Z. Luo, Z. Wang, Y. Huang, T. Tan, E. Zhou, Rethinking the heatmap regression for bottom-up human pose estimation, arXiv preprint (2021) .doi:10.48550/arXiv.2012.15175.
- [18] H. Qu, L. Xu, Y. Cai, L. G. Foo, J. Liu, Heatmap distribution matching for human pose estimation, arXiv preprint (2022) .doi:10.48550/arXiv.2210.00740.
- [19] D. Maji, S. Nagori, M. Mathew, D. Poddar, Yolo-pose: Enhancing yolo for multi person pose estimation using object keypoint similarity loss, arXiv preprint (2022) .doi:10.48550/arXiv.2204.06806.
- [20] D. Wang, S. Zhang, Spatial-aware regression for keypoint localization, Conference on Computer Vision and Pattern Recognition (2024) 624-633doi:10.1109/CVPR52733.2024.00066.
- [21] K. He, G. Gkioxari, P. Dollár, R. Girshick, Mask r-cnn, International Conference on Computer Vision (2017) 2980–2988doi:10.1109/ICCV.2017.322.
- [22] J. M. Molina, J. P. Llerena, L. Usero, M. A. Patricio, Advances in instance segmentation: Technologies, metrics and applications in computer vision, Neurocomputing 625 (2025) 129584. doi:10.1016/j.neucom.2025.129584.
- [23] Y. Alzahrani, B. Boufama, Biomedical image segmentation: A survey, SN Computer Science 2 (2021). doi:10.1007/s42979-021-00704-7.

- [24] R. Wang, T. Lei, R. Cui, B. Zhang, H. Meng, A. Nandi, Medical image segmentation using deep learning: A survey, *IET Image Processing* 16 (2022). doi:10.1049/ipr2.12419.
- [25] E. Shaheen, A. Leite, K. A. Alqahtani, A. Smolders, A. Van Gerven, H. Willems, R. Jacobs, A novel deep learning system for multi-class tooth segmentation and classification on cone beam computed tomography. a validation study, *Journal of Dentistry* 115 (2021) 103865. doi:10.1016/j.jdent.2021.103865.
- [26] G. Chandrashekar, S. AlQarni, E. E. Bumann, Y. Lee, Collaborative deep learning model for tooth segmentation and identification using panoramic radiographs, *Computers in Biology and Medicine* 148 (2022) 105829. doi:10.1016/j.combiomed.2022.105829.
- [27] R. Zheng, Y. Zheng, C. Dong-Ye, Improved 3d u-net for covid-19 chest ct image segmentation, *Scientific Programming* 2021 (1) (2021) 9999368. doi:10.1155/2021/9999368.
- [28] W. Chen, F. Yang, X. Zhang, X. Xu, X. Qiao, Mau-net: Multiple attention 3d u-net for lung cancer segmentation on ct images, *Procedia Computer Science* 192 (2021) 543-552. doi:10.1016/j.procs.2021.08.056.
- [29] Y. Xu, Z. Yang, J. Song, Dental landmark detection with attention mechanisms in deep convolutional neural networks, *IEEE Access* 8 (2020) 68528-68537. doi:10.1007/978-3-030-87202-1_46.
- [30] A. Vaswani, N. Shazeer, N. Parmar, J. Uszkoreit, L. Jones, A. N. Gomez, L. Kaiser, I. Polosukhin, Attention is all you need, *Advances in neural information processing systems* (2017) 5998-6008.
- [31] H. Dujic, O. Meyer, P. Hoss, U. C. Wölfle, A. Wülk, T. Meusbürger, L. Meier, V. Gruhn, M. Hesenius, R. Hickel, J. Kühnisch, Automated detection of periodontal bone loss on periapical radiographs by vision transformer networks, *Diagnostics* 13 (23) (2023) . doi:10.3390/diagnostics13233562.
- [32] K. Muhammed Sunnetci, S. Ulukaya, A. Alkan, Periodontal bone loss detection based on hybrid deep learning and machine learning models with a user-friendly application, *Biomedical Signal Processing and Control* 77 (2022) 103844. doi:10.1016/j.bspc.2022.103844.

- [33] A. Vollmer, M. Vollmer, G. Lang, A. Straub, A. Kübler, S. Gubik, R. C. Brands, S. Hartmann, B. Saravi, Automated assessment of radiographic bone loss in the posterior maxilla utilizing a multi-object detection artificial intelligence algorithm, *Applied Sciences* 13 (3) (2023) 1858. doi:10.3390/app13031858.
- [34] M. Liu, S. Wang, H. Chen, Y. Liu, A pilot study of a deep learning approach to detect marginal bone loss around implants, *BMC Oral Health* 22 (2022) . doi:10.1186/s12903-021-02035-8.
- [35] Z. Geng, C. Wang, Y. Wei, Z. Liu, H. Li, H. Hu, Human pose as compositional tokens, *Conference on Computer Vision and Pattern Recognition* (2023) 660-671doi:10.1109/CVPR52729.2023.00071.
- [36] Y. Ci, Y. Wang, M. Chen, S. Tang, L. Bai, F. Zhu, R. Zhao, F. Yu, D. Qi, W. Ouyang, Unihcp: A unified model for human-centric perceptions, *Conference on Computer Vision and Pattern Recognition* (2023) 17840-17852doi:10.1109/CVPR52729.2023.01711.
- [37] R. P. Danks, S. Bano, A. Orishko, H. J. Tan, F. Moreno Sancho, F. D’Aiuto, D. Stoyanov, Automating periodontal bone loss measurement via dental landmark localisation, *International Journal of Computer Assisted Radiology and Surgery* 16 (7) (2021) 1189-1199. doi:10.1007/s11548-021-02431-z.
- [38] J. Y. Cha, H. I. Yoon, I. S. Yeo, K. H. Huh, J. S. Han, Peri-implant bone loss measurement using a region-based convolutional neural network on dental periapical radiographs, *Journal of Clinical Medicine* 10 (5) (2021) . doi:10.3390/jcm10051009.
- [39] L. Kumaralingam, H. B. V. Dinh, K. C. T. Nguyen, K. Punithakumar, T. G. La, E. H. Lou, P. W. Major, L. H. Le, Detsegdiff: A joint periodontal landmark detection and segmentation in intraoral ultrasound using edge-enhanced diffusion-based network, *Computers in Biology and Medicine* 182 (2024) 109174. doi:10.1016/j.combiomed.2024.109174.
- [40] J. Chang, M. F. Chang, N. Angelov, C. Y. Hsu, H. W. Meng, S. Sheng, A. Glick, K. Chang, Y. R. He, Y. B. Lin, B. Y. Wang, S. Ayilavarapu, Application of deep machine learning for the radiographic diagnosis of

- periodontitis, *Clinical Oral Investigations* 26 (2022) . doi:10.1007/s00784-022-04617-4.
- [41] J. Terven, D. M. Córdova-Esparza, J. A. Romero-González, A comprehensive review of yolo architectures in computer vision: From yolov1 to yolov8 and yolo-nas, *Machine Learning and Knowledge Extraction* 5 (4) (2023) 1680-1716. doi:10.3390/make5040083.
- [42] T. Y. Lin, P. Dollar, R. Girshick, K. He, B. Hariharan, S. Belongie, Feature pyramid networks for object detection, *conference on computer vision and pattern recognition* (2017) 2117-2125doi:10.1109/CVPR.2017.106.
- [43] N. Carion, F. Massa, G. Synnaeve, N. Usunier, A. Kirillov, S. Zagoruyko, End-to-end object detection with transformers, *arXiv preprint* (2020) .doi:10.48550/arXiv.2005.12872.
- [44] W. Mao, Y. Ge, C. Shen, Z. Tian, X. Wang, Z. Wang, A. v. den Hengel, Poseur: Direct human pose regression with transformers, *European Conference on Computer Vision* 13666 (2022) 72-88. doi:10.1007/978-3-031-20068-7_5.
- [45] M. Tonetti, H. Greenwell, K. Kornman, Staging and grading of periodontitis: Framework and proposal of a new classification and case definition, *Journal of Periodontology* 89 (2018) S159-S172. doi:10.1002/JPER.18-0006.
- [46] A. Toshev, C. Szegedy, Deeppose: Human pose estimation via deep neural networks, *Computer Vision and Pattern Recognition* (2014) 1653–1660doi:10.1109/CVPR.2014.214.
- [47] T. Lin, M. Maire, S. Belongie, J. Hays, P. Perona, D. Ramanan, P. Dollár, C. L. Zitnick, Microsoft coco: Common objects in context, *European Conference on Computer Vision* (2014) 740-755doi:10.1007/978-3-319-10602-1_48.
- [48] Humans in the loop, teeth segmentation on dental x-ray images [dataset], *kaggle, v1* (2023). doi:10.34740/KAGGLE/DSV/5884500.

- [49] J. C. M. Román, V. R. Fretes, C. G. Adorno, R. G. Silva, J. L. V. Noguera, H. Legal-Ayala, J. D. Mello-Román, R. D. E. Torres, J. Facon, Panoramic dental radiography image enhancement using multi-scale mathematical morphology, *Sensors* 21 (9) (2021). doi:10.3390/s21093110.
- [50] B. Thanathornwong, S. Suebnukarn, Automatic detection of periodontal compromised teeth in digital panoramic radiographs using faster regional convolutional neural networks, *Imaging Science in Dentistry* 50 (2020) 169. doi:10.5624/isd.2020.50.2.169.
- [51] J. Krois, T. Ekert, L. Meinhold, T. Golla, B. Kharbot, A. Wittemeier, C. Dörfer, F. Schwendicke, Deep learning for the radiographic detection of periodontal bone loss, *Scientific Reports* 9 (2019) . doi:10.1038/s41598-019-44839-3.
- [52] S. Ren, K. He, R. Girshick, J. Sun, Faster r-cnn: Towards real-time object detection with region proposal networks, *Advances in Neural Information Processing Systems* 28 (2015) 91-99.
- [53] L. Jiang, D. Chen, Z. Cao, F. Wu, H. Zhu, F. Zhu, A two-stage deep learning architecture for radiographic staging of periodontal bone loss, *BMC Oral Health* 22 (2022) . doi:10.1186/s12903-022-02119-z.
- [54] J. H. Lee, D. h. Kim, S. N. Jeong, S. H. Choi, Diagnosis and prediction of periodontally compromised teeth using a deep learning-based convolutional neural network algorithm, *Journal of Periodontal and Implant Science* 48 (2018) 114. doi:10.5051/jpis.2018.48.2.114.
- [55] H. J. Chang, S. Lee, T. H. Yong, N. Y. Shin, B. G. Jang, J. E. Kim, K. H. Huh, S. S. Lee, M. S. Heo, S. C. Choi, T. I. Kim, W. J. Yi, Deep learning hybrid method to automatically diagnose periodontal bone loss and stage periodontitis, *Scientific Reports* 10 (2020) . doi:10.1038/s41598-020-64509-z.
- [56] M. Farhadian, P. Shokouhi, P. Torkzaban, A decision support system based on support vector machine for diagnosis of periodontal disease, *BMC Research Notes* 13 (2020) . doi:10.1186/s13104-020-05180-5.
- [57] N. Tsoromokos, S. Parinussa, F. Claessen, D. Anssari Moin, B. Loos, Estimation of alveolar bone loss in periodontitis using machine learning,

International Dental Journal 72 (2022) . doi:10.1016/j.identj.2022.02.009.

- [58] M. B. H. Moran, M. Faria, G. Giraldo, L. Bastos, B. d. S. Inacio, A. Conci, On using convolutional neural networks to classify periodontal bone destruction in periapical radiographs, International Conference on Bioinformatics and Biomedicine (2020) 2036-2039doi:10.1109/BIBM49941.2020.9313501.
- [59] S. Kida, T. Nakamoto, M. Nakano, K. Nawa, A. Haga, J. Kotoku, H. Yamashita, K. Nakagawa, Cone beam computed tomography image quality improvement using a deep convolutional neural network, Cureus 10 (2018) . doi:10.7759/cureus.2548.

Appendix .1. Test Metrics

Within Table .6 and Table .7, we report the 18 image holdout test performance metrics, including mAP^{.5}, mAP^{.5:.95}, precision, and recall, for both the bounding box and keypoints, respectively.

Metrics	Bounding Box Class					
	Single Root	Double Root	Triple Root	ARR	PLS	Average
mAP^{.5}	0.951 (±0.019)	0.810 (±0.024)	0.697 (±0.244)	0.467 (±0.106)	0.190 (±0.086)	0.623 (±0.296)
mAP^{.5:.95}	0.678 (±0.020)	0.579 (±0.036)	0.587 (±0.214)	0.231 (±0.060)	0.073 (±0.021)	0.430 (±0.256)
Precision	0.867 (±0.023)	0.794 (±0.064)	0.277 (±0.138)	0.353 (±0.144)	0.281 (±0.190)	0.515 (±0.290)
Recall	0.941 (±0.029)	0.746 (±0.044)	0.993 (±0.015)	0.467 (±0.163)	0.262 (±0.143)	0.682 (±0.297)

Table .6: Bounding box holdout test set metrics for YOLOv8-pose nano model on our dataset.

Metrics	Keypoint Classes Without Post-Processing											
	CEJ-m	BL-m	RL-m	CEJ-d	BL-d	RL-d	RL-c	FA	FBL-m	FBL-d	ARR	Average
PRCK^{0.5}	0.862 (±0.031)	0.948 (±0.012)	0.610 (±0.139)	0.993 (±0.008)	0.987 (±0.007)	0.667 (±0.174)	0.955 (±0.033)	0.627 (±0.134)	0.744 (±0.133)	0.767 (±0.146)	0.533 (±0.067)	0.906 (±0.019)
PRCK^{0.25}	0.760 (±0.055)	0.828 (±0.052)	0.522 (±0.151)	0.835 (±0.043)	0.855 (±0.026)	0.604 (±0.165)	0.955 (±0.033)	0.627 (±0.134)	0.744 (±0.133)	0.767 (±0.146)	0.533 (±0.067)	0.811 (±0.037)
PRCK^{0.05}	0.331 (±0.052)	0.353 (±0.027)	0.119 (±0.034)	0.283 (±0.066)	0.315 (±0.041)	0.100 (±0.000)	0.608 (±0.087)	0.311 (±0.106)	0.325 (±0.041)	0.303 (±0.057)	0.467 (±0.067)	0.347 (±0.043)
NME	0.243 (±0.040)	0.172 (±0.027)	0.620 (±0.187)	0.143 (±0.015)	0.142 (±0.016)	0.543 (±0.219)	0.113 (±0.056)	0.535 (±0.149)	0.375 (±0.132)	0.351 (±0.140)	0.273 (±0.027)	0.319 (±0.068)
Metrics	Keypoint Classes With Post-Processing											
	CEJ-m	BL-m	RL-m	CEJ-d	BL-d	RL-d	RL-c	FA	FBL-m	FBL-d	ARR	Average
PRCK^{0.5}	0.862 (±0.031)	0.952 (±0.018)	0.610 (±0.139)	0.996 (±0.007)	0.986 (±0.007)	0.667 (±0.174)	0.955 (±0.033)	-	-	-	-	0.908 (±0.020)
PRCK^{0.25}	0.727 (±0.047)	0.813 (±0.037)	0.522 (±0.151)	0.783 (±0.055)	0.820 (±0.042)	0.584 (±0.192)	0.932 (±0.033)	-	-	-	-	0.784 (±0.040)
PRCK^{0.05}	0.399 (±0.046)	0.392 (±0.042)	0.133 (±0.042)	0.389 (±0.075)	0.393 (±0.043)	0.106 (±0.006)	0.595 (±0.099)	-	-	-	-	0.397 (±0.026)
NME	0.250 (±0.039)	0.175 (±0.025)	0.618 (±0.189)	0.150 (±0.020)	0.146 (±0.019)	0.543 (±0.222)	0.124 (±0.057)	-	-	-	-	0.322 (±0.069)

Table .7: Keypoint holdout test metrics for YOLOv8-pose nano model with and without post-processing on our dataset. Metrics in bold indicate the better performing method.